Comparison of temperature distributions inside a PEM fuel cell with parallel and interdigitated gas distributors

J.J. Hwang [*], S.J. Liu

Department of Environment and Energy, National University of Tainan, Tainan 700, Taiwan

Abstract

A comparison of the temperature distributions in a proton exchange membrane (PEM) fuel cell between the parallel-flow gas distributors and the interdigitated gas distributor has been discussed in detail. An electrochemical–thermal coupled numerical model in a five-layer membrane-electrode assembly (MEA) is developed. The temperatures for the reactant fuels as well as the carbon fibers in the porous electrode are predicted by using a CFD technique. The overpotential across the MEA is varied to examine its effect on the temperature distributions of the PEM fuel cell. It is found that both the fuel temperature and the carbon fiber temperature are increased with increasing the total overpotential. In addition, the fuel and carbon-fiber temperature distributions are significantly affected by the flow pattern that cast on the gas distributor. Replacing the parallel-flow gas distributor by the interdigitated gas distributor will increase the local maximum temperature inside the PEM fuel cell.
© 2006 Elsevier B.V. All rights reserved.

Keywords: Proton exchange membrane fuel cell; Porous electrode; Darcy flow

1. Introduction

The majority of heat source in a proton exchange membrane (PEM) fuel cell are the irreversibility of electrochemical reactions as well as the Joule heat. It rises the fuel cell temperature during operation. The local temperature distribution inside a fuel cell has a strong impact on the fuel cell performance since it affects the water-vapor distribution by means of condensation. Insufficient cooling may result in local hot spots and thus dehydrate, shrink or even rupture the membrane. In addition, the kinetics of electrochemical reactions directly depends on temperature. Therefore, from the viewpoint of promotion in reliability, durability, and performance of PEM fuel cell, an efficient thermal management of a PEM fuel cell becomes crucial. It not only removes the generated heat from inside the fuel cell to the outside but also keep the spatial uniformity of temperature distribution that avoids local hot spots.

Some isothermal models have been developed for understanding the adiabatic mechanisms inside a fuel cell. One-dimensional models accounting for diffusive mass transport and electrochemical kinetics were developed by Bernardi and Verbrugge [1,2] and Springer et al. [3,4]. Two-dimensional models were developed by Nguyen and White [5], Fuller and Newman [6], and Gurau et al. [7]. Most of these assume some concentration profile of reactant species along the channel except for [7], which accounts directly for convective mass transport. Recently, Shimpalee and Dutta [8] described a steady state, isothermal, three-dimensional, and single phase PEM fuel cell model. It used a commercial code to solve the complete Navier–Stokes equations. Zhou and Liu [9], Um and Wang [10], and Hwang et al. [11] described a 3D model for PEM fuel cell. Their results agree well with the experimental observations. It is note that the above-modeled results are based on the adiabatic conditions.

This paper extends the author's previous work [12] about the cathodic thermal behaviors to study the thermal-transport phenomena in the entire membrane-electrode assembly of a PEM fuel cell. A two-equation model is employed to resolve the temperature difference between the carbon fibers and the fuels in the gas diffusion layer. In addition, conservations of mass, momentum, species and charge couple with the above thermal transports with proper account of electrochemical kinetics and fluid dynamics. A computational-fluid-dynamics methodology is used to integrate the above multi-physics transports of in a PEM fuel cell. The possibility of hot spot inside a fuel cell is

---

* Corresponding author. Fax: +886 422518272.
  E-mail address: azaijj@mail.nutn.edu.tw (J.J. Hwang).

Nomenclature

c_i	mole concentration of the species i (mol m^{-3}), $c_i = \left[(\omega_i/M_i)/\sum_j^N (\omega_j/M_j)\right](P/RT)$
D_i	diffusivity of species i ($\text{m}^2\,\text{s}^{-1}$)
F	Faraday's constant ($96{,}487\,\text{C mol}^{-1}$)
h_v	interfacial heat transfer coefficient (volumetric) ($\text{W m}^3\,\text{K}^{-1}$)
i	current density (A m^{-2})
j	transfer current density (A m^{-3})
k_c	thermal conductivity of the solid phase in the catalyst layer ($\text{W K}^{-1}\,\text{m}^{-1}$)
k_f	thermal conductivity of the fluid phase ($\text{W K}^{-1}\,\text{m}^{-1}$)
k_s	thermal conductivity of the solid phase ($\text{W K}^{-1}\,\text{m}^{-1}$)
M	molecular weight (kg mol^{-1})
p	pressure (Pa)
$p_{i,m}$	possibility of the electrolyte in the connection of the catalyst layer
$p_{i,s}$	possibility of the catalyst in the connection of the catalyst layer
R	universal gas constant ($\text{W mol}^{-1}\,\text{K}^{-1}$)
S	source terms in the governing equations
T	temperature (K)
$\mathbf{u}$	velocity vectors (m s^{-1})
x, y	coordinate system, Fig. 1 (m)

Greek symbols

α	symmetric factor
ε	porosity (gas diffusion layer)
ε_c	porosity of the catalyst layer
η_{tot}	total overpotential across the MEA (V)
κ	permeability (m^2)
μ	viscosity (m s^{-2})
ρ	density (kg m^{-3})
σ_m	ionic conductivity of the membrane phase ($\Omega^{-1}\,\text{m}^{-1}$)
σ_s	electric conductivity of the catalyst phase($\Omega^{-1}\,\text{m}^{-1}$)
τ	tortuosity
υ_m	volume fraction of the ionic conductor (electrolyte phase) in the catalyst layer
υ_s	volume fraction of the electric conductor (catalyst phase) in the catalyst layer
ϕ_m	potential of the ionic conductor (electrolyte phase) (V)
ϕ_s	potential of the electric conductor (catalyst phase) (V)
ω	mass fraction

Subscripts

a	anode
c	catalyst or cathode
e	energy
eff	effective
f	fluid
HOR	hydrogen oxidation reaction
i	species
j	electricity
m	membrane phase, momentum
o	exchange current density
ORR	oxygen reduction reaction
ref	reference
s	solid, catalyst phase
tot	total
T	transfer current

assessed by examine the effects of total overpotential and gas distributor geometry on the temperature distributions inside the PEM fuel cell. Moreover, the detailed temperature distributions inside a PEM fuel cell provide a comprehensive understanding of the mechanisms responsible for thermal pathways. It is helpful in the design of thermal management of a low-temperature fuel cell.

2. The model

A sectional view of a typical PEM fuel cell is given in Fig. 1. The model domain is confined within a five-layer MEA (membrane-electrode assembly), i.e., two gas diffusion layers (GDLs), two catalyst layers (CLs), and a proton exchange membrane (PEM). Each GDL is in contact with a gas distributor. Humidified hydrogen and saturated air are supplied to the anodic gas distributor and the cathodic gas distributor, respectively. In the anodic catalyst layer, hydrogen is consumed to form protons that carry the ionic current to the cathode. In the cathodic catalyst layer, the electrochemical reaction not only consumes the oxygen but also produces the water. The hydrogen oxidation reaction (HOR) in the anodic catalyst layer and the oxygen reduction reaction (ORR) in the cathodic catalyst layer are, respectively, expressed as by the following equations:

$$\frac{1}{2}H_2 \rightarrow H^+ + e^- \tag{1}$$

$$\frac{1}{4}O_2 + H^+ + e^- \rightarrow \frac{1}{2}H_2O \tag{2}$$
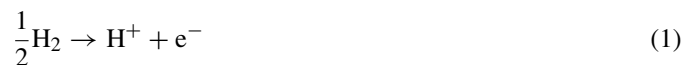
Both feeds are regarded as ideal gases and are transported through diffusion and convection. The electrodes are treated as homogeneous porous media with uniform morphological properties such as porosity and permeability. All gases within each of the electrodes exist as a continuous phase. In addition, water in the vapor phase is considered to simplify the model.

As shown in Fig. 2, two kinds of gas distributors are examined, i.e., the parallel-channel gas distributor (symmetric flow) and interdigitated gas distributor (asymmetric flow).
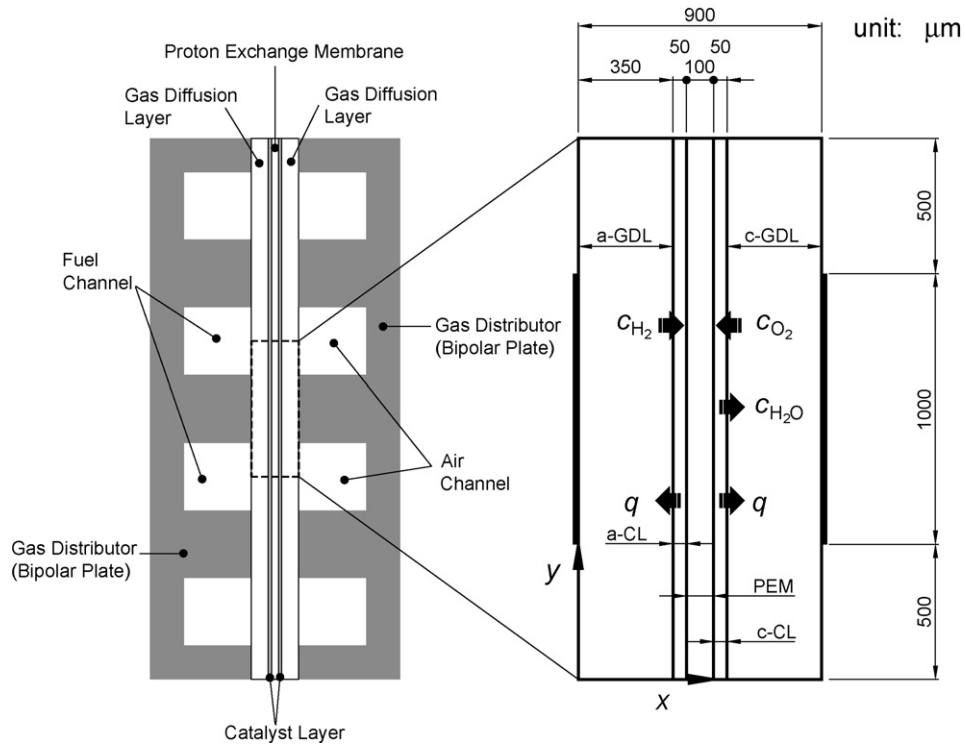
Fig. 1. Sectional view of the fuel cell module.

2.1. Governing equations

The ionic and electronic current balances in the PEM and GDLs, based on the Ohm's law, are respectively described as the following equations:

$$\nabla(-\sigma_m \nabla \phi_m) = 0 \tag{3}$$

$$\nabla(-\sigma_s \nabla \phi_s) = 0 \tag{4}$$

where ϕ_m and ϕ_s are the membrane-phase potentials and the catalyst-phase potentials, respectively. σ_m and σ_s are the ionic and electronic conductivities of the PEM and GDLs, respectively.

In the catalyst layer of a PEM fuel cell, the porous matrix contains two kinds of solid phases, i.e., ionic conductor (electrolyte) and electronic conductor (catalyst). A potential difference exists between the catalyst and electrolyte to drive the transfer current ($\mathbf{j}_T$), keeping the electrochemical reaction continuously. The current passes through catalyst layer can be decomposed two parts, i.e.:

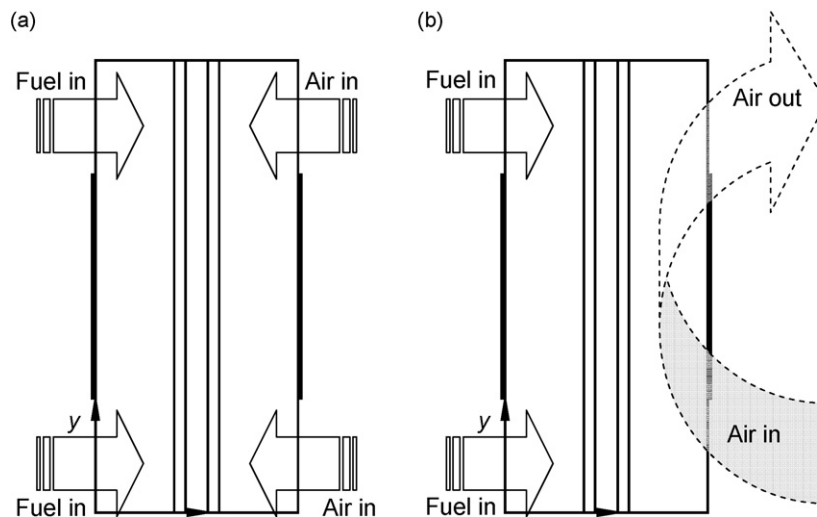$$\mathbf{i} = \mathbf{i}_s + \mathbf{i}_m \tag{5}$$

Fig. 2. Schematic drawings of the flow patterns of (a) parallel-channel gas distributor (symmetric flow) and (b) interdigitated-channel gas distributor (asymmetric flow).

where $\mathbf{i}_s$ and $\mathbf{i}_m$ are the currents flowing through the catalyst and the electrolyte, respectively. Since the electrodes are electroneutral everywhere, there is no charge-buildup in the catalyst layers. Thus, the charge conservation is:

$$\nabla \cdot \mathbf{i} = 0 \tag{6}$$

That is:

$$\nabla \cdot \mathbf{i}_s = -\nabla \cdot \mathbf{i}_m \tag{7}$$

These two current components interact through electrochemical reactions. The electrons are transferred to the catalyst from the electrolyte in the anodic catalyst layer, and vice versa in the cathodic catalyst layer. Application of Ohm's law to equation yields the current conservation:

$$\nabla \cdot (-\sigma_{s,eff} \nabla \phi_s) = -S_j \tag{8}$$

$$\nabla \cdot (-\sigma_{m,eff} \nabla \phi_m) = S_j \tag{9}$$

where the sources terms S_j and $-S_j$ are the local transfer current densities corresponds to the HOR and ORR in the anode and cathode, respectively, creating and consuming protons. They are denoted as $\mathbf{j}_{T,HOR}$ and $\mathbf{j}_{T,OOR}$, respectively, in the following discussion. $\sigma_{s,eff}$ and $\sigma_{m,eff}$ are the effective electronic and ionic conductivities of the catalyst and electrolyte, respectively. They are modeled as:

$$\sigma_{s,eff} = \sigma_s(1 - \varepsilon_c) \times \upsilon_s \times p_{i,s} \tag{10}$$

$$\sigma_{m,eff} = \sigma_m(1 - \varepsilon_c) \times \upsilon_m \times p_{i,m} \tag{11}$$

where υ_s and υ_m are the volume fraction of the catalyst and electrolyte in the catalyst layer, respectively. $p_{i,s}$ and $p_{i,m}$ are the possibilities of the catalyst and electrolyte in the connection of the catalyst layer, respectively [7,11]. It is noted that only a long-range connection of the same particles stretch through the entire catalyst layer ensures good conductivity.

The present model takes into account two species in the anode (H_2, H_2O), and three in the cathode (O_2, H_2O, N_2). The species transports based on the Stefan–Maxwell multi-component diffusion are given by the following equations:

$$\rho \mathbf{u} \cdot \nabla \omega_i = \nabla \cdot \left\{ \rho \omega_i \sum_{j=1}^{N} D_{i,eff,\,j} \left[\frac{M}{M_j} \left(\nabla \omega_j + \omega_j \frac{\nabla M}{M} \right) + (x_j - \omega_j) \frac{\nabla p}{p} \right] \right\} + S_i \tag{12}$$

The effective diffusivities of the species i in the porous electrode follows the Bruggemann model, i.e.:

$$D_{i,eff} = \varepsilon^\tau D_i \tag{13}$$

The source terms S_i represent the consumption of the reactants during the electrochemical reaction. It becomes $S_i = \mathbf{j}_{T,ORR} M_{O_2}/4F$ and $S_i = \mathbf{j}_{T,HOR} M_{H_2}/2F$ in the cathodic and anodic catalyst layers, respectively. In the gas diffusion layer it is nothing. According to the Butler–Volmer correlation [13], the relationship among the local transfer current density ($\mathbf{j}_T$), the reactant concentrations (c_i), and phase potentials (ϕ_s, ϕ_m) can

be described as the following equation:

$$\mathbf{j}_{T,OOR} = \mathbf{j}_{o,c} \left\{ \left(\frac{c_{O_2}}{c_{O_2,ref}} \right) \exp \left[\frac{4\alpha_c F}{RT} (\phi_m - \phi_s) \right] \right.$$
$$\left. - \left(\frac{c_{H_2O}}{c_{H_2O,ref}} \right)^2 \exp \left[\frac{4(1 - \alpha_c)F}{RT} (\phi_m - \phi_s) \right] \right\} \tag{14}$$

$$\mathbf{j}_{T,HOR} = \mathbf{j}_{o,a} \left\{ \left(\frac{c_{H_2}}{c_{H_2,ref}} \right)^2 \exp \left[\frac{4\alpha_a F}{RT} (\phi_s - \phi_m) \right] \right\} \tag{15}$$

where $\mathbf{j}_{o,c}$, and $\mathbf{j}_{o,a}$, are the cathodic and anodic exchange current densities, respectively.

The fluid flow in the porous media is described by the following equations:

$$\rho \mathbf{u} \cdot \nabla \mathbf{u} = -\nabla p + \nabla \cdot (\mu \nabla \mathbf{u}) + S_m \tag{16}$$

$$\nabla(\rho \mathbf{u}) = S_c \tag{17}$$

where ρ is the density, μ the viscosity, $\mathbf{u}$ the velocity vector, and p is the pressure. The source term in the momentum equations is based on the Darcy's law, representing an extra drag force proportional to fluid viscosity and velocity, and inversely proportional to the permeability of a porous medium, i.e., $S_m = -(\mu/\kappa)\mathbf{u}$, where κ is the permeability.

As for the energy equations, the two-equation model is used to describe the thermal behaviors in the gas diffusion layer. The energy equations for fluid and solid phases, respectively, are:

$$(\rho c_p)_f \mathbf{u} \cdot \nabla T_f = \nabla \cdot (k_{f,eff} \nabla T_f) - S_{e,GDL} \tag{18}$$

$$0 = \nabla \cdot (k_{s,eff} \nabla T_s) + S_{e,GDL} + S_\Omega \tag{19}$$

The source terms $S_{e,GDL}$ and S_Ω are the thermal interaction between the solid matrices and the fluids and the resistive heating, respectively. They are represented by $S_{e,GDL} = -h_v \cdot (T_s - T_f)$ and $S_\Omega = \mathbf{i}_s^2/\sigma_{s,eff}$, respectively. h_v is the interfacial heat transfer coefficient (volumetric) between the solid matrices and the reactants fluid in porous medium [14]. The effective thermal conductivities of both phases are respectively defined as:

$$k_{s,eff} = (1 - \varepsilon)k_s \tag{20}$$

$$k_{f,eff} = \varepsilon k_f \tag{21}$$

where k_s and k_f are the thermal conductivities of the solid matrix and the reactant fluid, respectively.

In the catalyst layer, the electrochemical reaction occurs at the interface of reactant fluid and catalyst. Physically, the fluid and solid phases in the catalyst layer have the same temperatures, i.e.:

$$(\rho c_p)_f \mathbf{u} \cdot \nabla T_f = \nabla \cdot (k_{c,eff} \nabla T_f) + S_{e,CL} + S_\Omega \tag{22}$$

$$T_f = T_s \tag{23}$$

In the present model, the radiation heat flux and the energy dissipation due to Joule heating are neglected. Therefore, the source term in the above equation can be represented by the overpotential heating by the electrochemical activation, i.e., $S_{e,CL} = \mathbf{j}_{T,HOR} \times (\phi_m - \phi_s)$ in the anodic catalyst layer and $S_{e,CL} = \mathbf{j}_{T,ORR} \times (\phi_s - \phi_m)$ in the cathodic catalyst layer, respectively. The effective thermal conductivity of the catalyst layer is determined by the following equation [12]:

$$k_{c,eff} = -2k_c + \frac{1}{(\varepsilon/(2k_c + k_f)) + ((1-\varepsilon)/3k_c)} \tag{24}$$

where k_c is the weight-averaged conductivity between the ionic conductor (such as Nafion^{TM}) and the electric conductor (such as Pt/C).

As for the PEM, a typical conduction equation is employed to describe the thermal behavior in the impermeable material, i.e.:

$$\nabla \cdot (k_m \nabla T_s) = 0 \tag{25}$$

where k_m is the thermal conductivity of the PEM.

Table 1
Porous-electrochemical properties of the present modeled fuel cell

Description		Unit	Value
Exchange current density	Anode, $\mathbf{j}_{o,a}$	A m^{-3}	5.0×10^3
	Cathode, $\mathbf{j}_{o,c}$	A m^{-3}	1.0×10^{-3}
Symmetric factor	Anode, α_a	–	1.0
	Cathode, α_c	–	0.5
Porosity	a-GDL, c-GDL, ε	–	0.5
	a-CL, c-CL, ε_c	–	0.5
Permeability	a-GDL, c-GDL, κ	m^2	1.57×10^{-12}
	a-GDL, c-GDL, κ_c	m^2	1.57×10^{-12}
Tortuosity	a-GDL, c-GDL, τ	–	1.5
	a-GDL, c-GDL, τ_c	–	1.5
Thermal conductivity	GDL, $k_{s,eff}$	W kg^{-1} K^{-1}	1.7
	PEM, k_m	W kg^{-1} K^{-1}	0.5
	Anode gas, $k_{f,eff}$	W kg^{-1} K^{-1}	0.182
	Cathode gas, $k_{f,eff}$	W kg^{-1} K^{-1}	0.051
Electric conductivity	GDL (electronic), σ_s	Ω^{-1} m^{-1}	300
	PEM (ionic), σ_m	Ω^{-1} m^{-1}	14.4
Inlet pressure	Anode, $p_{in,a}$	kPa	1.013×10^5
	Cathode, $p_{in,a}$	kPa	1.013×10^5
Mass flow rate	Anode	kg s^{-1}	1.19×10^{-6}
	Cathode	kg s^{-1}	2.98×10^{-5}
Species mass fraction at cathode inlet (saturated air at STP)	Oxygen, ω_{O_2}	–	21.7%
	Water, $\omega_{H_2O,c}$	–	2.1%
	Nitrogen, ω_{N_2}	–	77.2%
	Total	–	100%
Species mass fraction at anode inlet (saturated H$_2$ at STP)	Hydrogen, ω_{H_2}	–	76.5%
	Water, $\omega_{H_2O,a}$	–	23.5%
	Total	–	100%

2.2. Boundary conditions

The electrochemical and physical properties used in the calculation are given in Table 1. The temperatures for both feeds along with the surfaces of the gas distributor are fixed at 298 K. Both outlets of the module have an ambient pressure. The anode is supplied with the humidified hydrogen of mass fractions of 76.5%/23.5% for H$_2$/H$_2$O. The cathodic side feeds with the saturated air of 21.7%/2.1%/77.2% for O$_2$/H$_2$O/N$_2$, where N$_2$ is considered as an inert gas and serves as diluents. Reactants delivered to the cathode and anode are 2.98×10^{-5} and 1.19×10^{-6} kg s^{-1}, respectively. The difference of electronic-conductor potential (ϕ_s) between two contact surfaces between the electrodes and gas distributors represents the total overpotential (η_{tot}) across the five-layer MEA. The potential at the contact surfaces between the c-GDL and the current collector is arbitrarily chosen to be zero, while the total overpotential is used as boundary condition at the anodic current collector. For the rest of the boundaries they have either insulation or symmetry conditions.

2.3. Numerical schemes

The governing equations are numerically solved by the control-volume-based finite difference method [15]. The discretization procedure ensures conservation of mass, momentum, energy and concentration over each control volume. The upwind difference scheme is used to treat the velocity, while the central difference scheme is employed to discretize the fluid density, temperature, and species concentration. Momentum equations corresponding to two coordinates are solved, followed by a pressure correction equation that does the mass balance. Concentration transport equations are solved after the bulk flow calculation. Velocity control volumes are staggered with respect to the main control volumes, and coupling of the pressure and velocity fields is treated via the SIMPLER pressure correction
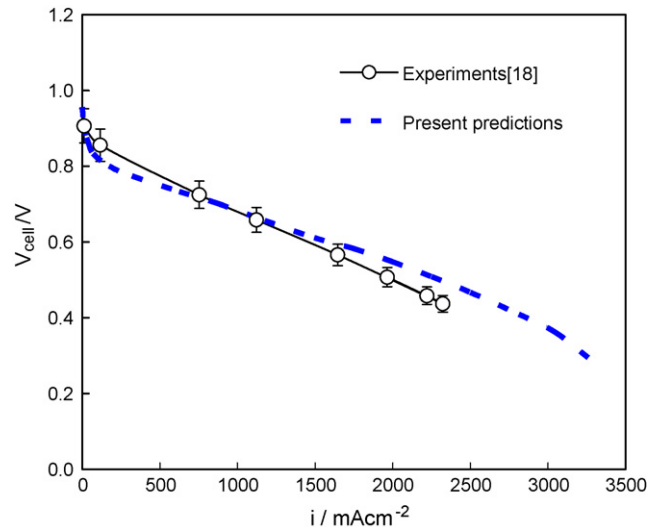

Fig. 3. Polarization-curve comparisons between the numerical results and previous experimental results.
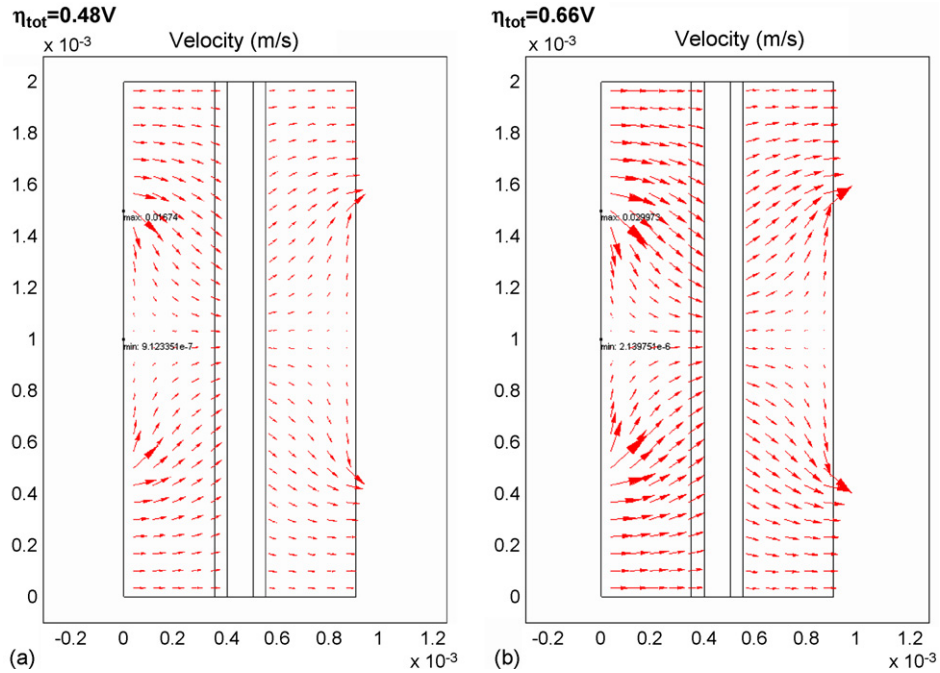
Fig. 4. Effect of overpotential on the flow velocities: dimensions in velocity, m s^{-1}; in length, *m*. (a) $\eta_{tot} = 0.48$ V and (b) $\eta_{tot} = 0.66$ V.

algorithm [15,16]. Obtaining new values for any desired variables, taking into account the latest known estimated values of the variable from the neighboring nodes solves the set of the differential equations over the entire region. One iteration process is complete when, in line-by-line technique, all lines in a direction have been accounted for. Because of the large variations in the source terms, under-relaxation is necessary for the dependent variables and the source terms to achieve convergence. Line inversion iteration with typical under-relaxation values of 0.1 for the velocity term and pressure correction terms is incorporated to the facilitated calculation [17]. Solutions are considered to be converged at each test condition after the ratio of residual source (including mass, momentum, energy and species) to the maximum flux across a control surface becomes below 1.03×10^{-6}.

In the present work, all computations are performed on 503,160 (*X* by *Y*) structured, orthogonal meshes. Additional runs for the coarser meshes, 403,120, and the finer meshes, 603,180, are taken for a check of grid independence. As shown in Fig. 3, the maximum discrepancies in the axial velocity and oxygen concentration profiles between two grid sizes of 503,160 and 603,180 are only 0.6% and 0.9%, respectively. In addition, results indicate a maximum change of 0.6 percent in wall temperature distribution between the solutions of 503,160 and 603,180 grids. All above discrepancies are so small that the accuracy of the solutions on a 503,160 grids is deemed satisfactory. The CPU time ranged from 3 to 6 h on a Pentium IV PC (2.8 GHz, 2GB RAM) using Windows XP operating system. Fig. 3 shows a flow chart of the present numerical modeling.
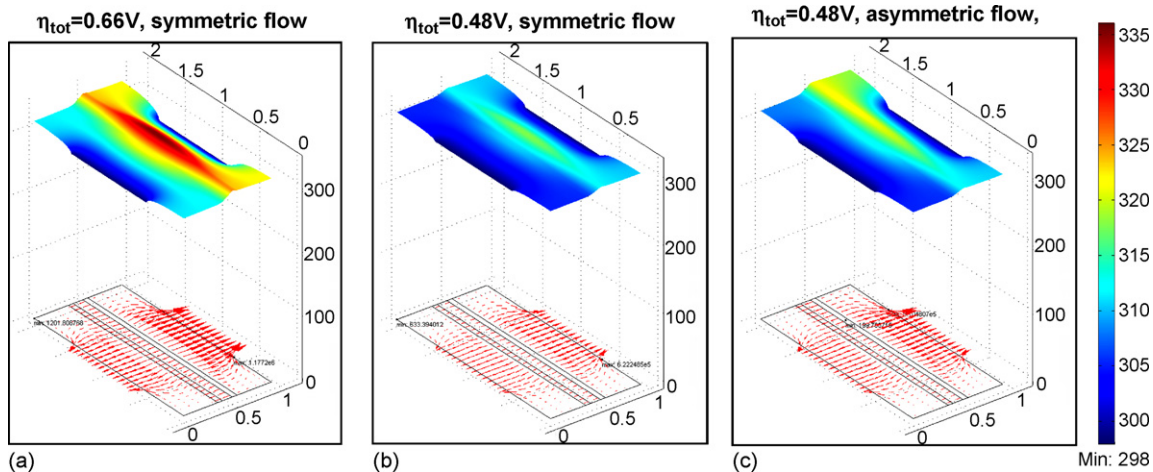

Fig. 5. Distributions of solid-phase temperatures and heat fluxes across the solid matrices: dimensions in temperature, K; in heat flux, W m^{-2}; in length, m. (a) $\eta_{tot} = 0.66$ V, symmetric flow, (b) $\eta_{tot} = 0.48$ V, symmetric flow, and (c) $\eta_{tot} = 0.48$ V, asymmetric flow.
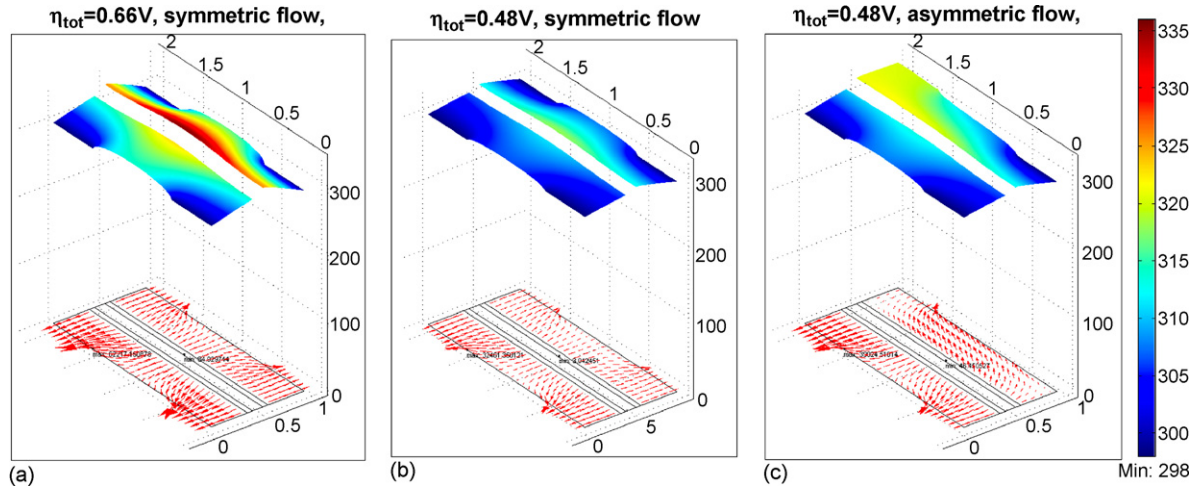
Fig. 6. Distributions of fluid-phase temperatures and the heat fluxes across the fluids: dimensions in temperature, K; in heat flux, W m^{-2}; in length, m. (a) $\eta_{tot} = 0.66$ V, symmetric flow, (b) $\eta_{tot} = 0.48$ V, symmetric flow, and (c) $\eta_{tot} = 0.48$ V, asymmetric flow.

3. Results and discussion

It is necessary to verify the present model prior to the discussion of the modeling results. To this aim, the authors have made a comparison of the I-V curve between the present numerical predictions with the experimental data [18]. As shown in Fig. 3, the agreement for the comparison is good, indicating that the present numerical results are reliable.

3.1. Thermal-fluid transports

Fig. 4(a) and (b) shows the flow-velocity vectors of $\eta_{tot} = 0.48$ and 0.66 V, respectively, for the symmetric-flow geometries. Two marks on each plot represent the local maximum and minimum velocities in the module. It is seen that the fuel side (anode) has flow velocities direct from the anodic flow channel toward the anodic catalyst layer. The maximum velocities occur at the inlet around the rib corners. The flow at about the middle of the rib surfaces ($y = 1.0$ mm) is nearly stagnant. In contrast, the velocities on the oxidant side direct from the cathodic catalyst layer toward to the flow channels. This is because the oxygen reduction reaction (Eq. (2)) in the cathodic catalyst layer not only consumes the oxygen but also produces the water vapor that acts as a mass source in the cathodic layer.

3D mappings of the solid-phase temperatures and the fluid-phase temperatures are shown in Figs. 5 and 6, respectively. The corresponding projects show the vectors of the heat fluxes across the solid matrices (Fig. 5) and the fluids (Fig. 6). Two point marks shown on each plot indicate the maximum or minimum heat fluxes in the module.

Fig. 5(a) and (b) shows the effect of total overpotential (η_{tot}) on the solid-phase temperature distributions for the symmetric-flow geometry. It is seen that the solid-phase temperature in the cathode is higher than that in the anode. This is because the c-CL dissipates more heat by the electrochemical reaction than the a-CL. The maximum temperature occurs at the middle of the module cutting across the
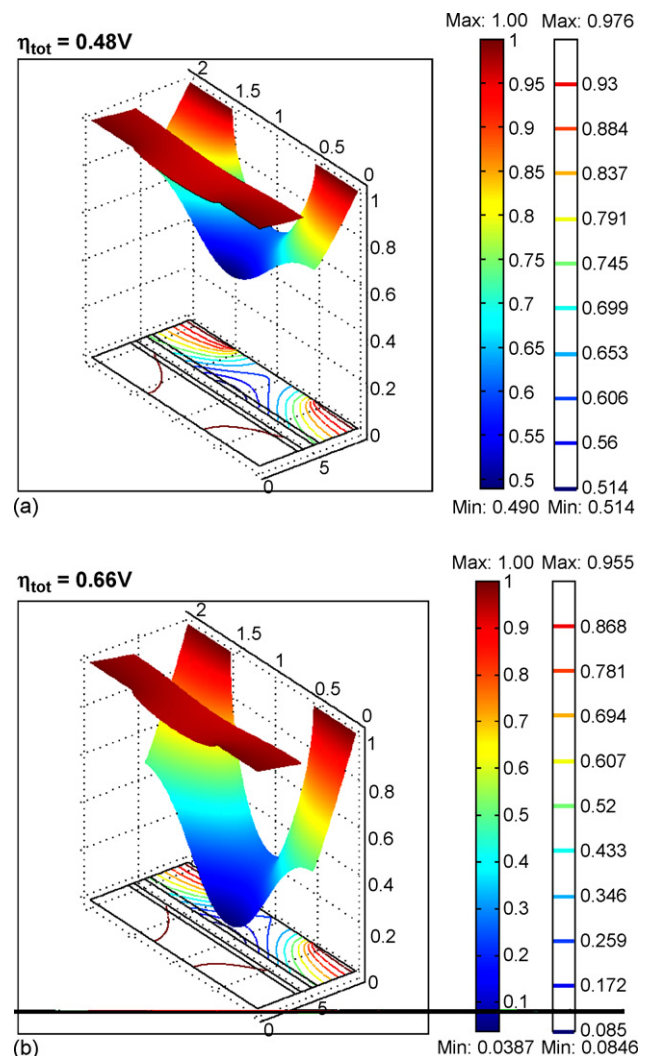

Fig. 7. Effect of overpotential on the reactant concentration distributions: (a) $\eta_{tot} = 0.48$ V and (b) $\eta_{tot} = 0.66$ V; dimensions in length, m.

cathodic catalyst layer ($y = 1.0$ mm). In addition, the region near the rib surface has a low solid-phase temperature. Near the fuel and oxidant entrances, the solid phase has low temperatures due to the convection by the cool inlet fluid. When the total overpotential reduces form $\eta_{tot} = 0.66$–0.48 V, as shown in Fig. 3, the solid-phase temperature distribution becomes more even. The maximum solid-phase temperature reduces from 336 to 317 K.

Fig. 5(c) shows the results of the asymmetric-flow geometry with the same total overpotential as that in Fig. 5(b). Again, the minimum solid-phase temperatures occur in the region near the rib surfaces ($y = 0$ and 0.9 mm). However, the maximum solid-phase temperature has been pushed downstream. The peak of the solid-phase temperature is increased from 317 to 323 K with the asymmetric-flow geometry instead of the symmetric-flow geometry. This is because the effect of overpotential heating near the cathode outlet becomes more significant due to the concentration polarization by depleting the oxidant.

Attention is turned to the heat fluxes across the solid matrices. It is seen that the vectors of heat fluxes direct from the catalyst layers toward to the surfaces of gas distributors. The gas distributors act as heat sinks to absorb the heat generated by the electrochemical reaction on the catalyst surfaces. Detailed inspection of these plots can get that the heat fluxes decrease with decreasing overpotential. In addition, the asymmetric flow (Fig. 5(c)) dissipated more heat than the symmetric flow (Fig. 5(b)). It is interesting to note that the significant heat produced by cathodic overpotential not only is conducted out by the cathodic gas distributor but also traverses the PEM and is removed by the anodic gas distributors.

Fig. 6 shows the fluid-phase temperature distributions in the GDL and CL. No data are displayed in the PEM (0.4 mm $< x < 0.5$ mm) because of its impermeability in nature. Again, the fluid-phase temperature in the cathode is higher than that in the anode. This is because the significant heat generation by the reaction in the cathodic catalyst layer. A faster electrochemical kinetics of HOR (i.e., higher exchange current density, Table 1) in the a-CL requires a less overpotential to drive the through-flow current in the fuel cell. Consequently, a less overpotential heating in the anodic catalyst layer results in a lower temperature. The fluid-phase temperature in the cathode increases downstream for the asymmetric-flow geometry due to the heat accumulation. The maximum fluid-phase temperature for the asymmetric-flow geometry is higher than the symmetric-flow geometry.

The heat transfer in the fluid phase is removed by both convection and conduction. Clearly, the heat transfer in the symmetric flows (Fig. 6(a) and (b)) is dominated by conduction. That is the heat flux from the catalyst layer direct toward to the flow channels. As for the cathode of the asymmetric flow, the convection dominates the heat transfer mechanism due to the high fluid velocity.

3.2. Species transports

Fig. 7 shows the effect of total overpotential on the concentration distribution in the module for the parallel-flow geometry. The data shown in the plots are normalized by the corresponding inlet concentration, i.e., $\omega_{H_2}/\omega_{H_2,in}$ for the anode and $\omega_{O_2}/\omega_{O_2,in}$ for the cathode. Comparing these two figures reveals
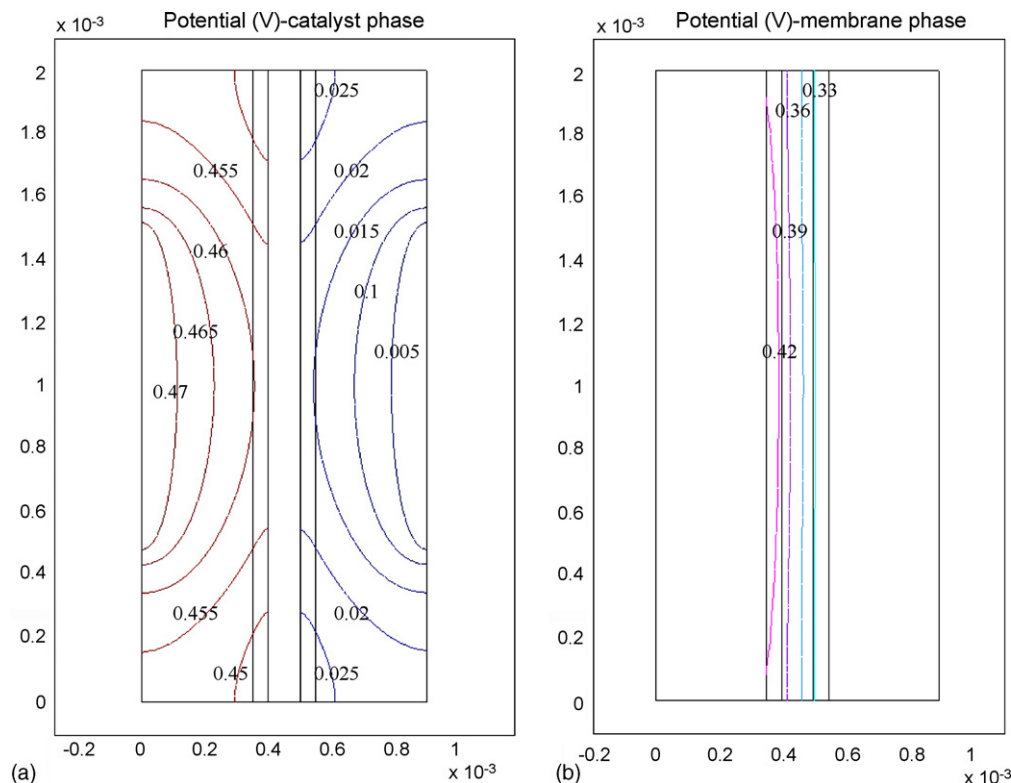

Fig. 8. Phase potential distributions in the fuel cell, $\eta_{tot} = 0.48$ V, dimensions in values, V.
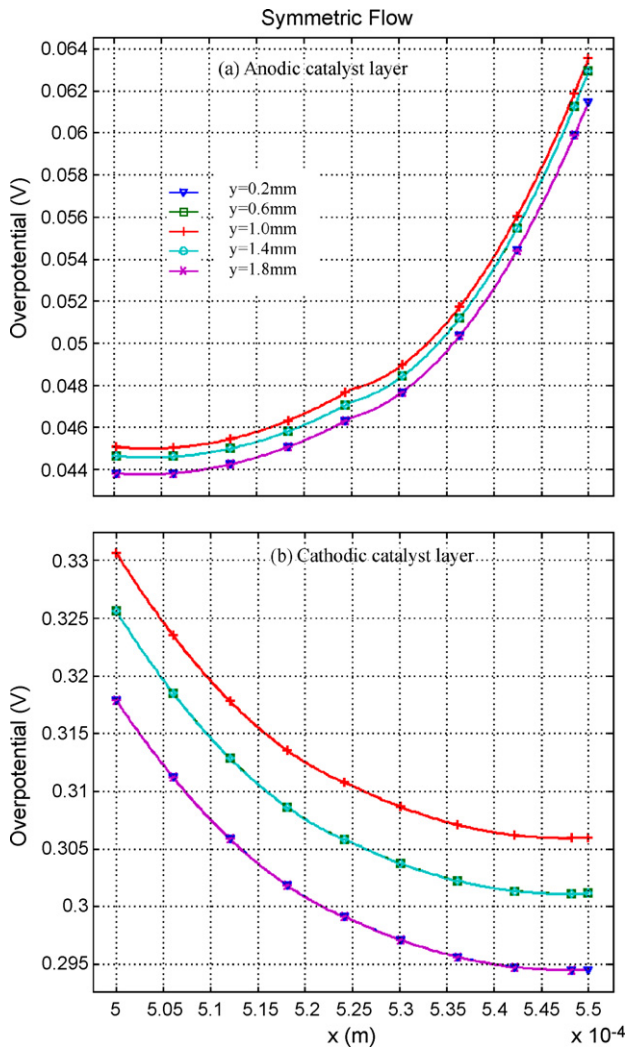
Fig. 9. Overpotential distributions in the catalyst layer, $\eta_{tot} = 0.48$ V, symmetric flow.
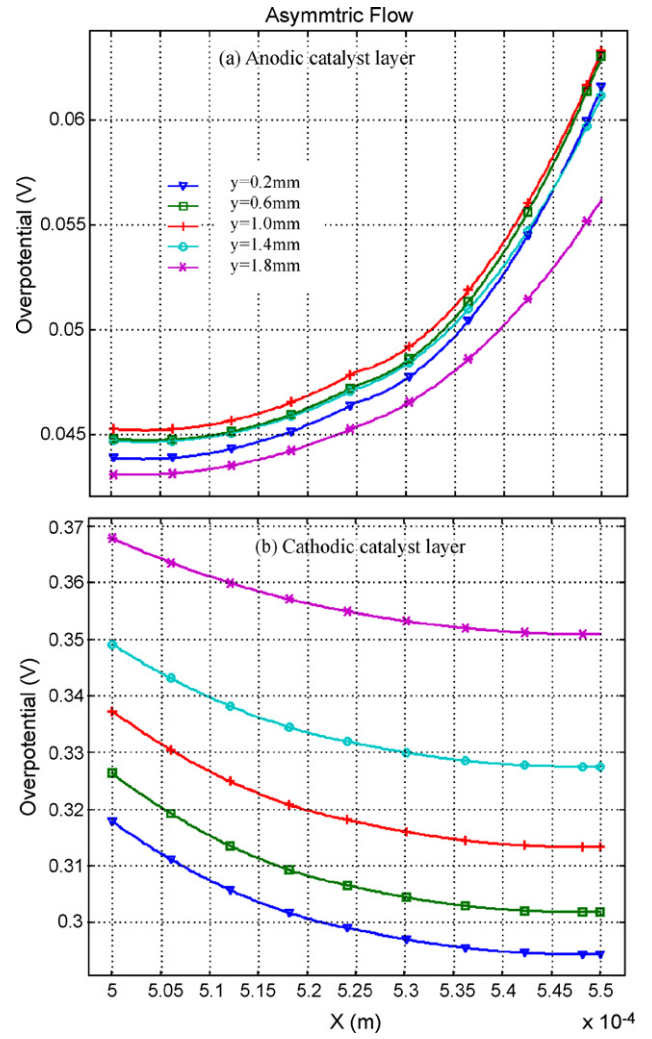

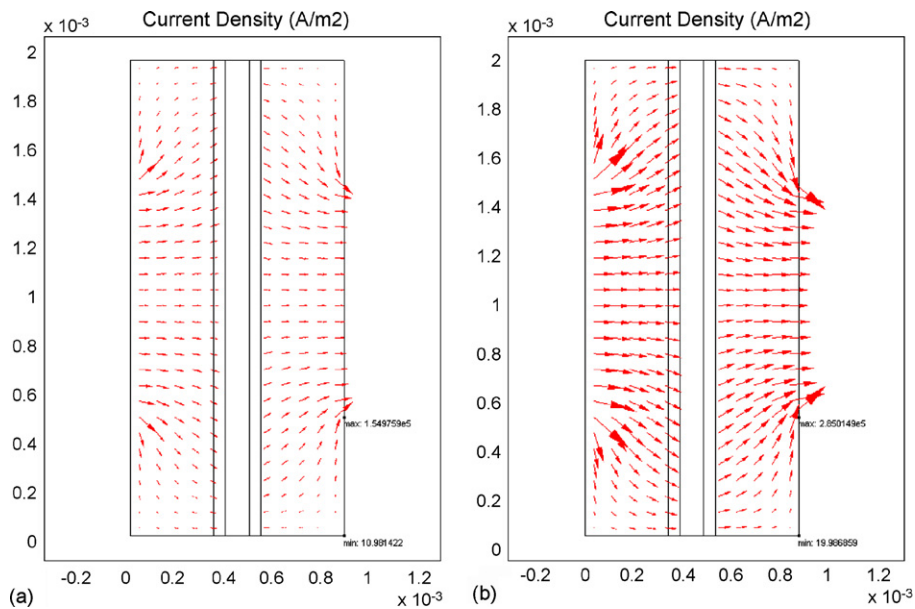Fig. 10. Overpotential distributions in the catalyst layer, $\eta_{tot} = 0.48$ V, asymmetric flow.

Fig. 11. Effect of overpotential on the current density distributions: dimensions in current density, A m^{-2}; in length, m.

that an increase of total overpotential increases the fuel and oxidant utilization in both electrodes. At a fixed total overpotential, the concentration decreases from the module entrance to the catalyst layer. A local minimum of the species concentration is found at the module middle in the catalyst layer. It is further seen that the concentration gradient along the x-direction in the cathode is more significant than that in the anode.

3.3. Electron transports

Fig. 8 shows the potential distributions of the catalyst phase ϕ_c (Fig. 8(a)) and membrane phase ϕ_m (Fig. 8(b)) in the fuel cell. The anode has a higher catalyst-phase than the cathode. It decreases along the x-direction to drive the electric current overcoming the Ohmic resistance. In the catalyst layer and the PEM, the membrane-phase potential has a relatively uniform distribution along y-direction. Again, the difference of the membrane-phase potential impels the ionic current through the PEM.

In the catalyst layers, the differences between the catalyst-phase potential and the membrane-phase potential represent the activation overpotentials, i.e., $\eta_a = \phi_c - \phi_m$ in the a-CL and $\eta_a = \phi_m - \phi_c$ in the c-CL. Figs. 9 and 10 show a comparison of the activation overpotential distributions at several elevations (y) between two different flow patterns. The activation overpotentials in both catalyst layers increases along the depth of the catalyst layer. That is the largest activation overpotentials occur at the both sides of the PEM. The activation overpotential in the c-CL is significantly higher than that in the a-CL for both flow patterns. The highest activation overpotential occurs at the module middle ($y = 0.1$ mm) for the symmetric flow, and the downstream station most for the asymmetric flow.

Fig. 11 shows the full-field distribution of the local current density in the module. It is seen that the current directs form the surfaces in contact with the anodic gas distributors toward the surfaces in contact with the cathodic gas distributors. The current density is high near the rib surface corner. It is further seen that the current density increases with increasing the total overpotential inside the fuel cell.

4. Concluding remarks

This paper has presented a comprehensive study on the thermal-transport behaviors in a PEM fuel cell. A multi-physics model is developed accounting for conservations of the co-transports of mass/momentum/heat/species/charge. In the gas diffusion layer, a two-equation thermal transport model is developed to cope with the local thermal non-equilibrium between the solid matrices and the fluids. In the catalyst layer, a general energy equation is derived using the volume-averaging technique, along with a local heat generation resulting from electrochemical reactions. Results show that both the solid-matrix temperature and the fluid temperature increase with increasing the total overpotential (η_{tot}). Under the same total overpotential, the maximum temperature is increased by replacing the symmetric-flow geometry with the asymmetric-flow geometry.

References

[1] D.M. Bernardi, M.W. Verbrugge, AIChE J. 37 (1991) 1151.
[2] D.M. Bernardi, M.W. Verbrugge, J. Electrochem. Soc. 139 (1992) 2477.
[3] T.E. Springer, T.A. Zawodinski, S. Gottesfeld, J. Electrochem. Soc. 136 (1991) 2334.
[4] T.E. Springer, M.S. Wilson, S. Gottesfeld, J. Electrochem. Soc. 140 (1993) 3513.
[5] T.V. Nguyen, R.E. White, J. Electrochem. Soc. 140 (8) (1993) 2178–2186.
[6] T.F. Fuller, J. Newman, J. Electrochem. Soc. 140 (5) (1993) 1218–1225.
[7] V. Gurau, H. Liu, S. Kakac, AIChE J. 44 (11) (1998) 2410–2421.
[8] S. Shimpalee, S. Dutta, Effect of Humidity on PEM Fuel Cell Performance. Part II. Numerical Simulation, HTD-vol. 364-1, Heat Transfer Division, ASME, 1999.
[9] T. Zhou, H. Liu, Int. J. Transport Phenom. 3 (3) (2001) 177–198.
[10] S. Um, C.Y. Wang, J. Electrochem. Soc. 147 (12) (2000) 4485–4493.
[11] J.J. Hwang, C.K. Chen, R.F. Savinell, C.C. Liu, J.C. Wainright, J. Appl. Electrochem. 34 (2004) 217.
[12] J.J. Hwang, P.Y. Chen, Int. J. Heat Mass Transfer 49 (2006) 2315.
[13] P. Costamagna, K. Honegger, J. Electrochem. Soc. 145 (1998) 3995.
[14] J.J. Hwang, G.J. Hwang, R.H. Yeh, C.H. Chao, J. Heat Transfer 124 (2002) 120.
[15] S.V. Patankar, Numerical Heat Transfer and Fluid Flow, Hemisphere, Washington, DC, 1980.
[16] J.J. Hwang, D.Y. Lai, Int. J. Heat Mass Transfer 41 (1998) 979–991.
[17] J.J. Hwang, J. Heat Transfer 120 (1998) 709–716.
[18] J.J. Hwang, J. Electrochem. Soc. 153 (2006) A216–A224.